

Synthetic Aperture Inversion for Arbitrary Flight Paths and Nonflat Topography

Clifford J. Nolan and Margaret Cheney

Abstract—This paper considers synthetic aperture radar (SAR) and other synthetic aperture imaging systems in which a backscattered wave is measured from positions along an arbitrary (known) flight path. We assume a single-scattering model for the radar data, and we assume that the ground topography is known but not necessarily flat.

We focus on cases in which the antenna footprint is so large that the standard narrow-beam algorithms are not useful. We show that certain artifacts can be avoided if the antenna and antenna footprint avoid particular relationships with the ground topography. In this case, we give an explicit backprojection imaging algorithm that corrects for the ground topography, flight path, antenna beam pattern, source waveform, and other geometrical factors.

For the case of a nondirectional antenna, the image produced by the above algorithm contains artifacts. For this case, we analyze the strength of the artifacts relative to the strength of the true image. The analysis shows that the artifacts can be somewhat suppressed by increasing the frequency, integration time, and the curvature of the flight path.

Index Terms—FOPEN, nonlinear flight path, synthetic aperture radar (SAR).

I. INTRODUCTION

IN synthetic aperture radar (SAR) imaging [8], [11], [13], [15], [39], a plane or satellite carrying an antenna moves along a flight path. The antenna emits pulses of electromagnetic radiation, which scatter off the terrain, and the scattered waves are measured with the same antenna. The received signals are then used to produce an image of the terrain. (See Fig. 1)

The nature of the imaging problem depends on the directivity of the antenna. We are interested particularly in the case of antennas with poor directivity, where the antenna footprint is large and standard narrow-beam imaging methods are not useful. This is typically the case for foliage-penetrating radar [38], [39], whose low frequencies do not allow for much beam focusing.

In the case of a nondirectional antenna on a straight-line flight track above a flat earth, it is not possible to determine from the data whether a given reflection originated from the left or the right side of the flight track. This gives rise to an image

Manuscript received October 17, 2001; revised February 21, 2003. This work was supported in part by the National Science Foundation through the Engineering Research Centers Program under Award EEC-9986821 and the Focused Research Groups in the Mathematical Sciences Program. The associate editor coordinating the review of this manuscript and approving it for publication was Dr. Mark A. Richards.

C. J. Nolan is with the Department of Mathematics & Statistics, University of Limerick, Limerick, Ireland (e-mail: clifford.nolan@ul.ie).

M. Cheney is with the Department of Mathematical Sciences, Rensselaer Polytechnic Institute, Troy, NY 12180 USA (e-mail: cheney@rpi.edu).

Digital Object Identifier 10.1109/TIP.2003.814243

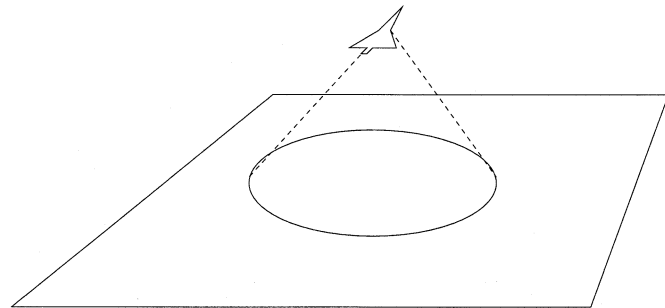


Fig. 1. Acquisition geometry for SAR with an antenna with poor directivity.

artifact which we call an *ambiguity artifact*. Similar ambiguity artifacts arise in the case of curved flight paths and nonflat earth topography. One goal of this paper is to give conditions on the relationship between the antenna footprint, the flight path, and the topography for which these ambiguity artifacts do not arise.

We consider imaging methods based on backprojection. Such methods produce an image I via

$$I(z) = \int w(z, s, t) d(s, t) ds dt \quad (1)$$

where d denotes the data, which depends on time t and a flight path parameter s , and w denotes a weighting function that will be explained in the text. This weighting function w depends on factors such as the flight path and the topography, and compensates for the antenna beam pattern, the source waveform, and other geometrical factors.

For an imaging formula such as (1), the image I is related to the desired ground reflectivity function V by

$$I(z) = \int K_I(z, x) V(x) d^2x. \quad (2)$$

In the case in which ambiguity artifacts can be avoided, we show that K_I is approximately a delta function. Consequently, the image I has the property that certain features such as edges and boundaries between different materials are positioned correctly and have the correct amplitudes.

In the case when ambiguity artifacts are unavoidable, we analyze the strength of these artifacts relative to the strength of the true image. Our analysis shows that the artifacts can be suppressed to some degree by increasing the curvature of the flight track, increasing the frequency, and increasing the integration time.

The paper is organized as follows. Section II introduces the mathematical model and relevant notation. Section III-A develops the image formation process, explains how the weight w

should be chosen, gives conditions for avoiding ambiguity artifacts, and displays computational examples showing the importance of the correct weighting factor w . Section III-B analyzes the case in which ambiguity artifacts are unavoidable and gives examples showing how the artifact is smeared as the curvature of the flight path is increased.

The paper concludes with two appendices. The first states the stationary phase theorem, which is used repeatedly in the paper, and gives some technical details regarding one of the conditions on the relationship between the topography and the flight path. The second appendix outlines the formulas used to generate the computational examples.

The methods we use in this paper are based on microlocal analysis [12], [18], [35], which is a theory for dealing with oscillatory integrals and singularities. These microlocal methods enable us to reconstruct edges and boundaries between different materials in the scattering region [3], [4], [6], [22], [26], [29], [30]. These edges and boundaries correspond mathematically to singularities in the reflectivity function; an image of these singularities gives us an image of structures such as walls and vehicles. The microlocal approach has the advantage of providing reconstruction formulas even in the case when the data are incomplete and nonideal. In addition, these methods can accommodate the varying antenna beam patterns that arise in the cases of nonideal antenna motion and gain, and with appropriate adjustments the same reconstruction formulas apply to both spotlight-mode [9] and stripmap-mode radar [13], [15]. Microlocal reconstruction techniques have been used to advantage in the geophysics community, where they have been found to be fast and robust [4], [6].

Microlocal methods have the limitation that they can only be expected to provide a reconstruction of singularities and their strengths. However, in practice they often reduce to the exact inversion formulas that are known for idealized cases. This is the case here: our reconstruction formula reduces to the exact inversion formula of [14], [19], [25] for the case of a perfect point source moving along a single straight flight track above a flat earth.

We use the capital letters X and Y for spatial variables in \mathbf{R}^3 , when there is danger of confusion between two-dimensional and three-dimensional vectors; x and y denote two-dimensional vectors corresponding to X and Y .

II. MATHEMATICAL MODEL

For SAR, the correct model is of course Maxwell's equations, but the simpler scalar wave equation is commonly used

$$\left(\nabla^2 - \frac{1}{c^2(X)}\partial_t^2\right)u(t, X) = 0 \quad (3)$$

where c is the wave propagation speed. Each component of the electric and magnetic fields in free space satisfies (3); thus it is a good model for the propagation of electromagnetic waves in dry air.

We assume the earth's surface is located at the position given by $X = \psi(x)$, where $\psi : \mathbf{R}^2 \rightarrow \mathbf{R}^3$ is known. Because electromagnetic waves are rapidly attenuated in the earth, we assume

that the scattering takes place in a thin region near the surface; thus we assume that the perturbation in wave speed c is of the form $c_0^{-2} - c^{-2}(X) = V(x)\delta(X - \psi(x))$. Here c_0 is the speed of light in dry air, and V , the *ground reflectivity function*, is the quantity we wish to image.

We show in [28] that the received field at sensor location Y and time t can be approximated by the expression

$$S(Y, t) = \int e^{-i\omega\left(\frac{t-2|\psi(x)-Y|}{c_0}\right)} W(x, Y, t, \omega) V(x) d\omega d^2x \quad (4)$$

where ω denotes the angular frequency; W contains geometrical factors such as the antenna beam pattern and the r^{-2} attenuation from geometrical spreading, and includes also the Fourier transform of the time-domain waveform sent to the sensor. Because this waveform is bandlimited, ultimately we reconstruct band-limited approximations to singularities rather than the actual singularities.

The idealized inverse problem is to determine V from knowledge of S for $t \in (T_1, T_2)$ and for Y on a curve. This curve we parametrize by $\gamma := \{\gamma(s) : s_{\min} < s < s_{\max}\}$. We will write $R_{s,x} = \psi(x) - \gamma(s)$.

The abrupt ends of the curve γ tend to cause artifacts in the image; consequently it is useful to multiply the data by a smooth taper $m(s, t)$ which is zero outside the region in (s, t) -space where we have data. The taper function must have an additional property: it should also be zero on the set $\{(s, t) : \text{for some } x, t = 2|R_{s,x}|/c_0 \text{ and } R_{s,x} \cdot D\psi(x) = 0\}$, where $D\psi$ denotes the 3×2 Jacobian matrix. In other words, we must avoid local minima of the traveltime. This assumption, which for example in the flat-topography case prevents us from trying to image directly under the antenna, is needed to avoid a number of technical difficulties.

We denote the map from scene V to data $d = ms$ by F , where

$$\begin{aligned} d &= F[V](s, t) \\ &= \int e^{-i\omega\left(\frac{t-2|R_{s,x}|}{c_0}\right)} A(x, s, t, \omega) V(x) d\omega d^2x \end{aligned} \quad (5)$$

where $A = mW$ [28].

We need the following assumption in order to make various stationary phase calculations hold; in fact this assumption makes the "forward" operator F a Fourier Integral Operator [12], [18], [35].

Assumption: The amplitude A of (5) satisfies

$$\sup_{(s,t,x) \in K} \left| \partial_\omega^\alpha \partial_s^\beta \partial_t^\delta \partial_{x_1}^{\rho_1} \partial_{x_2}^{\rho_2} A(x, s, t, \omega) \right| \leq C (1 + \omega^2)^{\frac{(2-|\alpha|)}{2}} \quad (6)$$

where K is any compact subset of $\mathbf{R}_s \times \mathbf{R}_t \times \mathbf{R}_x^2$, and the constant C depends on K , α , β , δ , ρ_1 , and ρ_2 .

This assumption is valid, for example, when the source waveform is a short pulse and the antenna is sufficiently broadband. We note that A can be complex; it can thus be used to model nonideal antenna behavior such as phase aberrations and frequency-dependent changes in the beam pattern.

III. IMAGE FORMATION

We form the image by means of a *filtered backprojection* operator

$$I(z) := \int Q(z, s, t, \omega) e^{i\omega \left(\frac{t-2|R_{s,z}|}{c_0} \right)} d(s, t) d\omega ds dt \quad (7)$$

where Q is determined below.

To determine Q , we investigate the degree to which the image I faithfully reproduces features of the ground reflectivity function V . We will show that under favorable circumstances, singular features such as edges appear in the correct locations.

Using $d = F[V]$ in (7) results in an equation of the form (2), where

$$K_I(z, x) = \int Q(z, s, \omega) e^{i\omega \left(\frac{t-2|R_{s,z}|}{c_0} \right)} \cdot e^{-i\tilde{\omega} \left(\frac{t-2|R_{s,x}|}{c_0} \right)} A(x, s, t, \tilde{\omega}) d\tilde{\omega} d\omega ds dt. \quad (8)$$

The kernel K_I is the imaging *point-spread function*, which, when considered as a function of the variable z , is the reconstructed (backprojected) image due to a delta point source located at x . If we had $K_I(z, x) = \delta(z - x)$, then the image I would be perfect; we want to determine Q so that K_I comes as close as possible to being a delta function.

In (8), we perform a large- ω stationary phase calculation in the variables $\tilde{\omega}$ and t . (Specifically, we make the change of variables $\tilde{\omega} = \omega v$ and perform a large- ω stationary phase calculation in the variables v and t . A statement of the multi-dimensional stationary phase theorem is given in Appendix A.) After substituting the stationary phase result into (8) and (2), we obtain

$$I(z) = \int K(z, x) V(x) dx + E_1(z) \quad (9)$$

where E_1 denotes a function smoother than the first term on the right side of (9) and

$$K(z, x) = 2\pi \int e^{\frac{i2\omega(|R_{s,x}| - |R_{s,z}|)}{c_0}} Q(z, s, \omega) \cdot A\left(x, s, \frac{2|R_{s,x}|}{c_0}, \omega\right) d\omega ds. \quad (10)$$

The main contributions to K come from those critical points of its phase at which the amplitude A is nonzero; the criticality conditions are

$$\begin{aligned} |R_{s,z}| &= |R_{s,x}| \\ \widehat{R}_{s,z} \cdot \dot{\gamma}(s) &= \widehat{R}_{s,x} \cdot \dot{\gamma}(s). \end{aligned} \quad (11)$$

The first condition of (11) says that x should be at the same range as z . The second says that the direction $\widehat{R}_{s,x}$ should have the same projection onto the flight velocity vector as the direction $\widehat{R}_{s,z}$.

Definition: We will call (s, x, z) a *contributing critical point* if it satisfies both conditions of (11) and if $A(x, s, 2|R_{s,x}|/c_0, \omega)$ is nonzero for some ω (and hence, by assumption (6), for a large interval of ω).

For a high-fidelity image, we would like K to be as close as possible to the delta function $\delta(z-x) \propto \int \exp(i(z-x) \cdot \xi) d\xi$. In

particular, we should have contributing critical points only when $z = x$. In other words, if (s, x, z) satisfies (11) when $z \neq x$, the amplitude A should be zero there. Flight paths for which this is the case can be found when the antenna beam pattern is sufficiently focused to one side of the flight heading.

For example, in the case of flat topography, there are points (s, x, z) satisfying (11) in two cases, one when $z = x$ and the other when z is at a “mirror” point x^* , which is the reflection of x across the horizontal projection of the line tangent to the flight path at $\gamma(s)$. This “mirror” critical point contributes to the image, and hence gives rise to an ambiguity artifact, unless the amplitude A is zero there. To make the amplitude A zero at all such “mirror” points, the antenna beam should be negligible to one side of the flight direction [16].

We show in the next section that the conditions for obtaining an image that is faithful (in a specific sense discussed below) are the following:

- 1) the only contributing critical points are those for which $z = x$;
- 2) at no point x in the antenna footprint should the earth’s surface be perpendicular to the plane formed by the range vector $R_{s,x}$ and the flight velocity vector $\dot{\gamma}(s)$. This should hold for every position $\gamma(s)$ along the flight path.

If condition 1 is violated, ambiguity artifacts appear in the image. If condition 2 is violated, “layover” occurs in the image: nearby points on the earth’s surface are mapped to the same point in the image [15].

We show in Section III-A that when the above conditions are satisfied, the point spread function K is, to leading order in ω , a band-limited delta function. This implies that the image formed by (7) exhibits the same singularities (such as edges) that are visible in the scene V . Moreover, the strengths of these singularities (such as the magnitude of the jump across an edge) is preserved in the image.

A. Case of No Ambiguity Artifacts

We show in this section that under the above conditions for avoiding ambiguity artifacts, a certain change of variables makes the phase of $K(z, x)$ the same as that of the delta function $\delta(z - x) \propto \int \exp(i(z - x) \cdot \xi) d\xi$.

1) *Change of Variables:* To determine the change of variables that makes the phase of K into the phase of a delta function, we first use the integral form of the remainder for Taylor’s theorem to write the imaginary part of the exponent of (10) as

$$\frac{2\omega(|R_{s,x}| - |R_{s,z}|)}{c_0} = (z - x) \cdot \Xi(z, x, s, \omega). \quad (12)$$

Explicitly, Ξ is given by

$$\Xi(z, x, s, \omega) = -\frac{2\omega}{c_0} \int_0^1 \nabla |R_{s,y}| \Big|_{y=x+\lambda(z-x)} d\lambda \quad (13)$$

where the differentiation on the right side is with respect to y , so that $\nabla R_{s,y} = \widehat{R}_{s,y}$. When $z = x$, (13) is simply

$$\Xi(z, z, s, \omega) = \left(\frac{-2\omega}{c_0} \right) \widehat{R}_{s,z} \cdot D\psi(z). \quad (14)$$

In a neighborhood of $z = x$, we make the change of variables

$$(s, \omega) \rightarrow \xi = \Xi(z, x, s, \omega). \quad (15)$$

For the case of straight flight paths, this change of variables is essentially the same change of variables used in ω - k migration [10], [23]. We do not actually use this change of variables to form the image; instead we form the image by (7) and use the change of variables only to determine the correct form of the amplitude Q . We note that this change of variables (15) can be done for any flight path, provided the Jacobian determinant (see below) is nonzero.

The change of variables (15) transforms the integral (9) into

$$I(z) = 2\pi \int e^{i(z-x)\cdot\xi} Q(z, s, \omega) A\left(x, s, \frac{2|R_{s,x}|}{c_0}, \omega\right) \cdot \left| \frac{\partial(s, \omega)}{\partial\xi} \right| (z, x, s, \omega) V(x) d^2\xi d^2x + E_1(z) \quad (16)$$

where s and ω are understood to refer to $s(\xi)$ and $\omega(\xi)$, respectively. This exhibits the operator with kernel K as a pseudodifferential operator. Pseudodifferential operators have the *pseudolocal* property [35], i.e., they do not move singularities or change their orientation.

The (absolute value of the) Jacobian determinant $|\partial(s, \omega)/\partial\xi|$ is also called the *Beylkin determinant* [4], [6]. When $x = z$, its reciprocal is given by

$$\left| \frac{\partial\xi}{\partial(s, \omega)} \right| (z, z, s, \omega) = \frac{4\omega}{c_0^2} \left| \begin{array}{cc} -\widehat{R}_{s,z} \cdot \frac{\partial\psi(z)}{\partial z_1} & P_{\perp} \dot{\gamma}(s) \cdot \frac{\partial\psi(z)}{\partial z_1} \\ -\widehat{R}_{s,z} \cdot \frac{\partial\psi(z)}{\partial z_2} & P_{\perp} \dot{\gamma}(s) \cdot \frac{\partial\psi(z)}{\partial z_2} \end{array} \right| \quad (17)$$

where $P_{\perp} \dot{\gamma}(s)$ denotes the scaled projection of $\dot{\gamma}(s)$ onto the plane perpendicular to $\widehat{R}_{s,z} \cdot \psi(z)$:

$$P_{\perp} \dot{\gamma}(s) = \frac{\dot{\gamma}(s) - \widehat{R}_{s,z} \left(\widehat{R}_{s,z} \cdot \dot{\gamma}(s) \right)}{|\widehat{R}_{s,z}|}. \quad (18)$$

We note that $P_{\perp} \dot{\gamma}(s)$ remains in the plane $T_{s,z}$ defined by

$$T_{s,z} := \text{Span} \{ \widehat{R}_{s,z}, \dot{\gamma}(s) \}. \quad (19)$$

Conditions under which the change of variables (15) can be made (locally) are those under which the right side of (17) is nonzero; this gives us the second condition on the relation between the flight track and the ground topography. This condition can be understood by noting that the vectors $\widehat{R}_{s,z}$ and $P_{\perp} \dot{\gamma}(s)$ are orthogonal and thus determine a coordinate system in the plane $T_{s,z}$; the rows of (17) are the coordinates of the tangent vectors $X^1 = \partial\psi/\partial z_1$ and $X^2 = \partial\psi/\partial z_2$ in this coordinate system. Thus the right side of (17) is nonzero provided X^1 and X^2 project to two linearly independent vectors in the plane $T_{s,z}$. In Appendix A, we show that this condition is equivalent to the condition that the earth's surface at z not be orthogonal to the plane $T_{s,z}$.

a) *Example: flat topography:* In the case of flat topography, the tangent line to the flight track (whose direction is

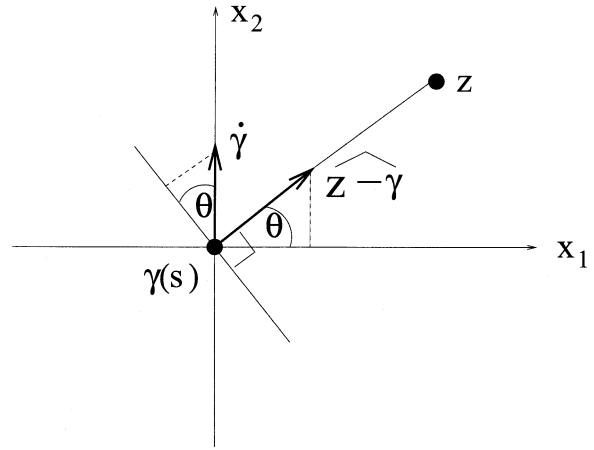


Fig. 2. Geometry for the Beylkin determinant for the flat-topography, straight-flight-path case.

given by the flight velocity vector) projects to a straight line on the earth. If the antenna's footprint is strictly to one side of this line, then contributing critical points occur only when $z = x$. If, in addition, the flight velocity vector is never vertical, then the plane $T_{s,z}$ is never vertical, and thus condition 2 for avoiding ambiguity artifacts is satisfied.

For flat topography, the Jacobian matrix $D\psi$ is simply

$$D\psi = \begin{pmatrix} 1 & 0 \\ 0 & 1 \\ 0 & 0 \end{pmatrix} \quad (20)$$

which implies that $\Xi(z, z, s, \omega) = (-2\omega/c_0) P_{1,2} \widehat{R}_{s,z}$, where $P_{1,2}$ denotes the operator that projects a three-dimensional vector onto its first two components.

b) *Example: flat topography, straight flight path:* Previous work [1], [19], [25] has considered the purely two-dimensional case in which the flight track is the x_2 axis. In this case, $D\psi$ is the 2×2 identity matrix; the two columns of (17) are orthogonal, and the first is a unit vector. The determinant is therefore the magnitude of the second vector, which is $|P_{\perp} \dot{\gamma}| = (\cos\theta)/|R_{s,z}|$, where θ is the angle formed by the flight track $\dot{\gamma}$ (the x_2 axis) and the line perpendicular to $R_{s,z}$. From Fig. 2 we see also that $\cos\theta = z_1/|R_{s,z}|$. Then, from (14), we have that $|\xi_1| = (2\omega/c_0)|\cos\theta|$. Thus on the diagonal $z = x$, the reciprocal of the Beylkin determinant is

$$\left| \frac{\partial\xi_1}{\partial(s, \omega)} \right| (z, z, s, \omega) = \frac{2\xi_1}{c_0|R_{s,z}|} = \frac{4\omega}{c_0^2} \frac{z_1}{|R_{s,z}|}. \quad (21)$$

c) *Example: flat topography, circular flight path:* Circular flight paths have been considered in [31]. For a flight path that is a circle of radius R in a plane at height H with arc-length parameterization, at the origin we have

$$\Xi(0, 0, s, \omega) = \frac{-2\omega R}{c_0(R^2 + H^2)^{1/2}} \left(\cos\left(\frac{s}{R}\right), \sin\left(\frac{s}{R}\right) \right) \quad (22)$$

which implies that the magnitude of the Beylkin determinant at the origin is $|\partial\xi/\partial(s, \omega)|(0, 0, s, \omega) = \frac{4\omega R}{c_0^2(R^2 + H^2)}$.

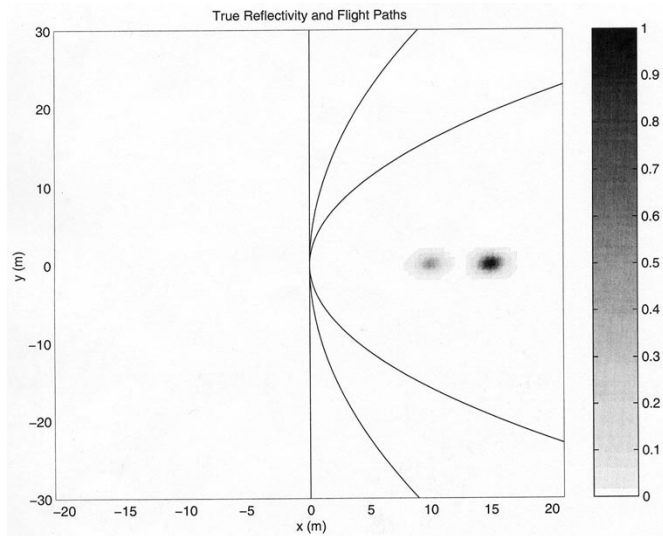


Fig. 3. Test scene and three flight paths.

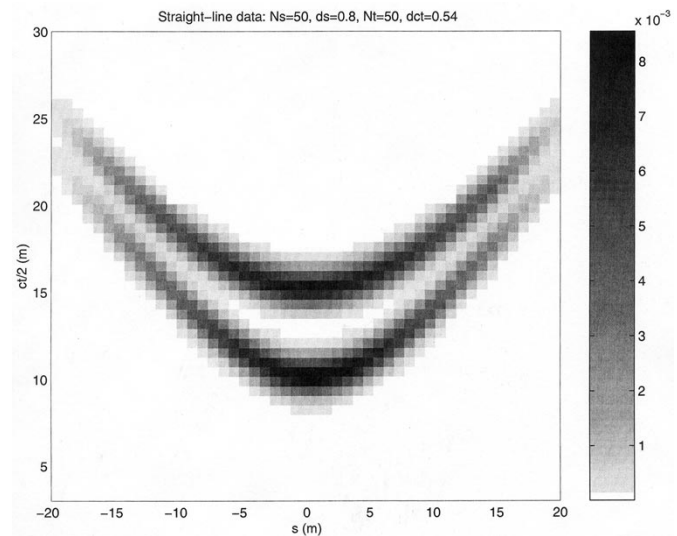


Fig. 4. Synthetic data for a straight flight track flight.

2) *Choice of the Amplitude Q* : Equation (16) shows how we should choose Q to make K an approximate delta function. In particular, we should choose

$$Q(z, s, \omega) = \frac{1}{(2\pi)^3} \frac{\chi(z, \xi(s, \omega))}{b(z, z, \xi(s, \omega))} \quad (23)$$

where χ is a smooth cutoff function that prevents us from dividing by zero, and where

$$b(z, x, \xi(s, \omega)) = A \left(x, s, \frac{2|R_{s,x}|}{c_0}, \omega \right) \left| \frac{\partial(s, \omega)}{\partial \xi} \right| (z, x, s, \omega). \quad (24)$$

With the choice (23) and change of variables (15), (10) becomes

$$K(z, x) = \frac{1}{(2\pi)^2} \int e^{i(z-x)\cdot\xi} \frac{b(z, x, \xi)}{b(z, z, \xi)} \chi(z, \xi) d^2 \xi. \quad (25)$$

Since the leading order contribution to (25) is at $z = x$, we see that K is an approximate delta function.

d) *Example: flat topography, straight flight track*: For the purely two-dimensional case of a straight flight track along the x_2 axis, the b that should be used in (23) is

$$b(z, z, \xi) = \frac{c_0 |R_{s,z}| A(z, s, \frac{2|R_{s,z}|}{c_0}, \omega)}{2\xi_1} \quad (26)$$

where it is understood that the ω and s appearing on the right side of (26) is shorthand notation for the functions $\omega(\xi)$ and $s(\xi)$. The corresponding filter used in [1], [19], [25] is, in the notation used here, simply $b^{-1}(z, z, \xi) = \xi_1$; this is the same as (26) up to the factors that are ignored in [1], [19], [25], such as $2/c_0$, the geometrical factor W , the source waveform, and the taper m . Thus we see that in this case, formula (7) reduces to the exact inversion formula.

3) *Numerical Examples*: Fig. 3 shows a test scene, for a flat earth, on which are superimposed the flight paths we use in this paper. We assume a perfect isotropically radiating antenna, so that $A \equiv 1$. Fig. 4 shows synthetic data generated from this scene. Fig. 5 shows the reconstruction when the Beylkin determinant is omitted; Fig. 6 shows the reconstruction including the

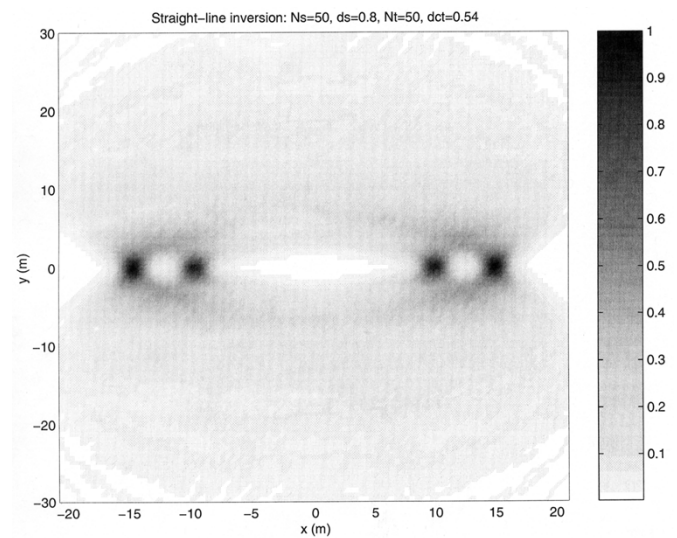


Fig. 5. Reconstructed image when the Beylkin determinant is omitted. Note the ambiguity artifacts here and in Fig. 6.

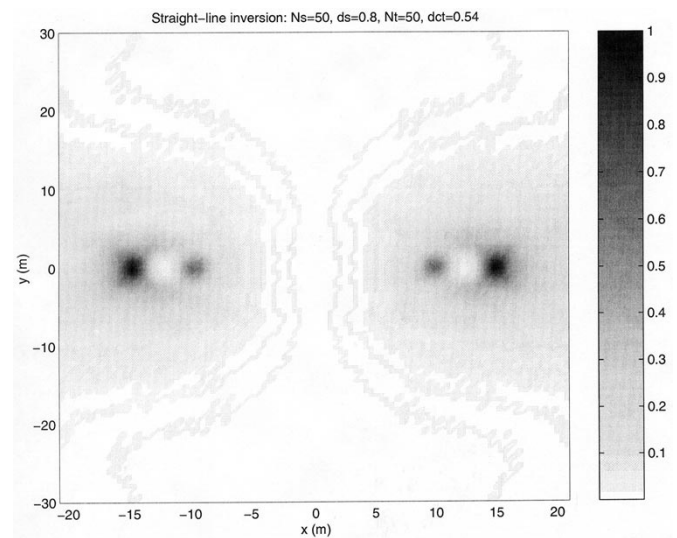


Fig. 6. Reconstructed image when the Beylkin determinant is included. Note that the strength of the weaker target is more nearly correct than in Fig. 5.

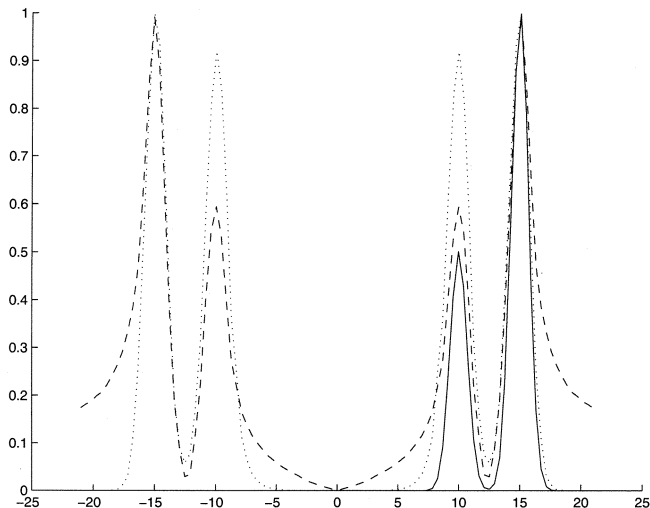


Fig. 7. Slices through the images of Figs. 3 (solid line), 5 (dotted line), and 6 (dashed line).

Beylkin determinant. All images have been normalized so the maximum reflectivity is 1. Fig. 7 shows a comparison of slices through all three images.

Fig. 7 shows that including the Beylkin determinant results in an image whose reflectivities are (almost) in the correct relation to each other, whereas omitting the determinant results in an image in which the relationship is incorrect.

We note that a straight flight path and isotropic antenna radiation pattern results in artifacts that are perfectly symmetrical with respect to the flight path.

B. Ambiguity Artifacts

In this section, we discuss the effect of an antenna with poor directivity, where (11) has more than one solution in the support of A .

We form an image by the same filtered backprojection method (7) as in the high-directivity case. In other words, we use the same Beylkin determinant weighting for the whole image, even though this determinant does not correspond to the change of variables (15) when $z \neq x$.

1) *Analysis:* As before, the main contributions to K come from the critical points (11) in the support of A .

In the flat-earth case, we saw that there are two points z on the earth for which (s, z, x) satisfies (11): one at $z = x$, which gives rise to the correct image, and one at a “mirror” point, which can give rise to an artifact. For nonflat topography, it is possible (see Fig. 8) to have a curve of points z on the earth for which (s, z, x) satisfies (11). Such a curve is composed of points at the same range $|R_{s,z}|$ whose directions $\widehat{R}_{s,z}$ have the same projection onto the flight velocity vector $\dot{\gamma}(s)$.

We refer to contributing critical points for which $z \neq x$ as “extraneous” critical points; it is these critical points that give rise to the ambiguity artifacts. We analyze the relative contributions to the image from these points by investigating the size of K there.

At an extraneous critical point (s, z, x) , we consider the kernel of (10), and carry out a large- ω stationary phase analysis in the s variable. We denote by ϕ the phase of (10).

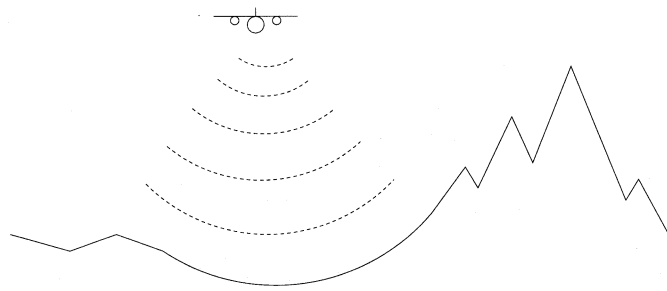


Fig. 8. Case when there is a curve of points z on the ground for which (s, z, x) is critical. In this slice, the entire valley floor consists of critical points.

We can carry out the stationary phase reduction with respect to s at an extraneous critical point only when the Hessian of the phase function with respect to s is nondegenerate. At a point satisfying both equations of (11), this Hessian is

$$\phi''(z, s, x) = 2 \left(\widehat{R}_{s,z} - \widehat{R}_{s,x} \right) \cdot \frac{\dot{\gamma}(s)}{c_0}. \quad (27)$$

We note that this Hessian is always zero when $x = z$; thus this stationary phase reduction can never be done at the true image point. Similarly, the Hessian is always zero for a straight flight path (assuming that s is an arc-length parameterization).

On the other hand, if the earth and flight track are level, and the flight track is curved, then $\widehat{R}_{s,z} - \widehat{R}_{s,x}$ is roughly co-linear with $\dot{\gamma}(s)$, so that the Hessian ϕ'' is nonzero at extraneous critical points. In this section, we consider the generic case when the Hessian is nonzero.

At extraneous critical points $s(z, x)$ for which the Hessian is nonzero, we can apply to the stationary phase theorem (see Appendix A). We obtain to leading order of approximation

$$K(z, x) \approx \frac{e^{i\frac{\pi}{4}}}{(2\pi)^{\frac{3}{2}}} \int \frac{1}{|\omega|^{\frac{1}{2}}} \frac{A\left(x, s, \frac{2|R_{s,x}|}{c_0}, \omega\right)}{A\left(z, s, \frac{2|R_{s,z}|}{c_0}, \omega\right)} \cdot \frac{\chi(z, \xi(s, \omega))}{|\phi''|^{\frac{1}{2}}(z, x, s)} \left| \frac{\partial \xi}{\partial(s, \omega)} \right| (z, z, s, \omega) d\omega \quad (28)$$

where s is understood to refer to $s(z, x)$, which is determined by solving the second equation of (11) for s in a neighborhood of a point (s, z, x) for which (11) holds.

On the other hand, if we consider the reconstruction at x we find

$$K(x, x) \approx \frac{1}{(2\pi)^2} \int \chi(x, \xi(s, \omega)) \cdot \left| \frac{\partial \xi}{\partial(s, \omega)} \right| (x, x, s, \omega) d\omega ds \approx \frac{1}{(2\pi)^2} \int \chi(x, \xi) d\xi. \quad (29)$$

Equations (28) and (29) tell us the degree to which a point scatterer at x creates an artifact at the point z . We see that the strength of the artifact at z can be decreased by increasing ϕ'' ; ϕ'' can be increased by increasing the curvature of the flight track. The strength of the true image at x , moreover, can be increased by increasing the length of the flight path for which x is in the antenna footprint (i.e., increasing the integration time).

2) Special Cases:

a) *Straight flight path:* The stationary phase reduction (28) cannot be carried out for a straight flight path; if the an-

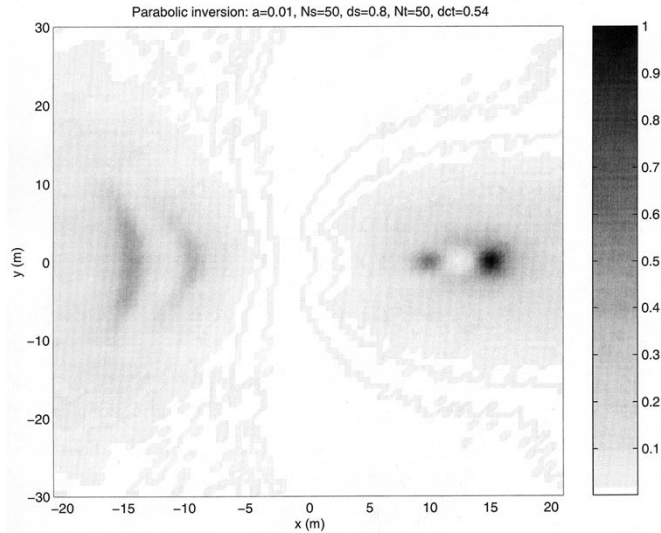


Fig. 9. This shows the reconstructed image from the flight path $x = .01y^2$. Note that the artifacts are weaker and more smeared than in Fig. 6.

tenna beam pattern is isotropic, then by symmetry the artifacts are symmetric with respect to the flight path. Fig. 6 shows an example of this phenomenon.

b) Circular flight path: For a flight path that is an arc of length L of a circle with radius R and an isotropic antenna beam pattern, a scatterer at the origin gives rise to artifacts that form a circular arc with radius $2R$. We can calculate the strength of these artifacts by computing $\dot{\gamma}(s) = -(\hat{R}(s)/R)$, where $\hat{R}(s) = (\cos(s/R), \sin(s/R), 0)$, $\hat{R}_{s,z} - \hat{R}_{s,0} = 2R(R^2 + H^2)^{-1/2}\hat{R}(s)$, and $\phi''(z, s, 0) = -(4/c_0)(R^2 + H^2)^{-1/2}$. Thus the artifacts, to leading order, have strength

$$K(z, 0) \approx \frac{2Re^{i\pi/4}}{(2\pi c_0)^{3/2}(R^2 + H^2)^{3/4}} \int \omega^{1/2} d\omega. \quad (30)$$

The image at the origin, on the other hand, is (to leading order)

$$\begin{aligned} K(0, 0) &\approx \frac{1}{(2\pi)^2} \int \frac{4\omega R}{c_0^2(R^2 + H^2)} d\omega ds \\ &\approx \frac{4LR}{(2\pi c_0)^2(R^2 + H^2)} \int \omega d\omega. \end{aligned} \quad (31)$$

We see that the ratio of artifact to true image is

$$\frac{|K(z, 0)|}{|K(0, 0)|} \approx \frac{2(2\pi c_0)^{1/2}(R^2 + H^2)^{1/4}}{3L} \frac{\omega_M^{3/2} - \omega_m^{3/2}}{\omega_M^2 - \omega_m^2} \quad (32)$$

where ω_M and ω_m denote the (effective) maximum and minimum angular frequencies of the radar. We see that the artifact can be minimized by increasing the curvature (decreasing R), increasing the path length L , lowering the flight path, and increasing the frequency.

3) Numerical Examples: Fig. 9 shows a reconstruction from the slightly curved flight path visible in Fig. 3; Fig. 11 shows a reconstruction from the more curved path. We see that as the curvature of the flight path increases, the artifacts become weaker and less localized. The weaker artifacts for the flight path with higher curvature are predicted by (28).

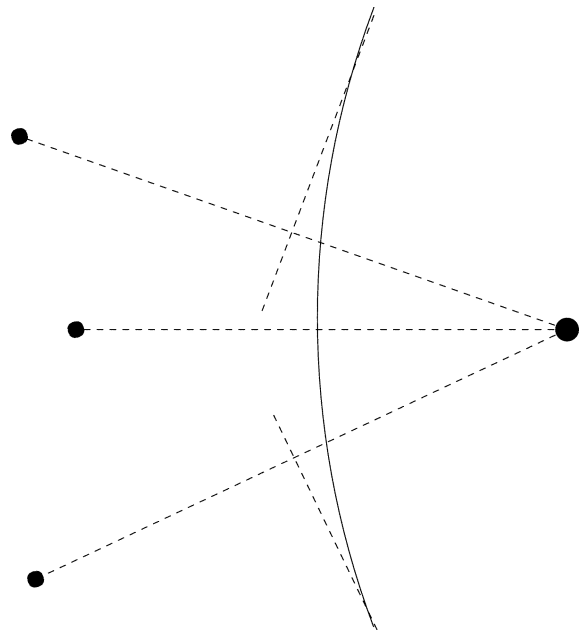


Fig. 10. This shows how a flight path curving to the right can cause an artifact curving to the left. A contribution to the artifact appears reflected about the tangent line.

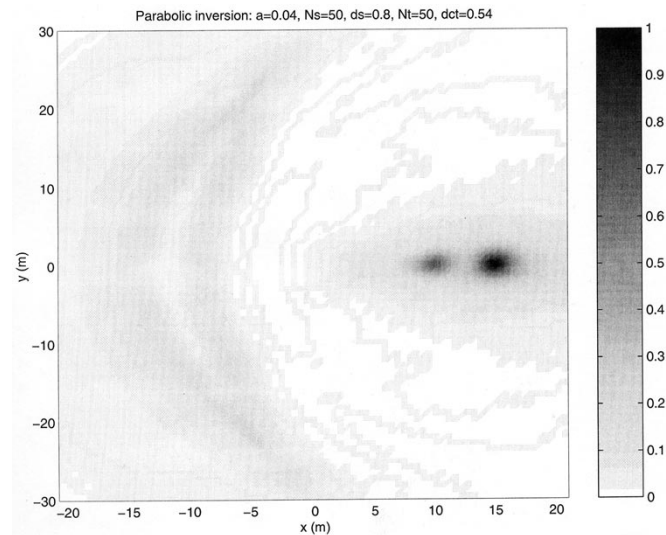


Fig. 11. This shows the reconstructed image from the flight path $x = .04y^2$. The artifacts are weaker and more smeared than in either Fig. 6 or Fig. 9.

Fig. 10 shows how it is possible for a flight path curving to the right to cause artifacts that curve to the left.

IV. CONCLUSIONS

We have exhibited a filtered backprojection algorithm for SAR imaging from arbitrary (known) flight paths and nonflat (known) earth topography. The analysis has given conditions on the relationship between the flight path, the antenna beam pattern, and the earth topography under which the image contains no ambiguity artifacts and no layover artifacts. When these conditions are satisfied, backprojection produces an image in which edges appear in the correct position and orientation; with the proper filter, jumps across edges are also of the correct magnitude. When the flight path, antenna beam

pattern, and earth topography are such that ambiguity artifacts are present, the strength of these artifacts can be affected by the curvature of the flight path, path length (integration time), and frequency. More highly curved flight paths smear the artifacts and decrease their magnitude.

We leave to the future the problem of finding an algorithm to pick out a flight path that minimizes the ambiguity artifacts.

APPENDIX A SOME TECHNICAL DETAILS

A. Method of Stationary Phase

The stationary phase theorem [5], [18] states

Theorem: If a is a smooth function of compact support on \mathbf{R}^n , and ϕ has only nondegenerate critical points, then as $\omega \rightarrow \infty$

$$\int e^{i\omega\phi(x)} a(x) d^n x = \sum_{\{x^0: D\phi(x^0)=0\}} \left(\frac{2\pi}{\omega}\right)^{\frac{n}{2}} e^{i\omega\phi(x^0)} \cdot a(x^0) \frac{e^{\frac{i\pi \operatorname{sgn} D^2\phi(x^0)}{4}}}{\sqrt{|\det(D^2\phi(x^0))|}} + O(\omega^{-\frac{(n-2)}{2}}) \quad (33)$$

where $D\phi$ denotes the gradient of ϕ and $D^2\phi$ denotes the Hessian.

B. Conditions on Planes

We denote by P_{\perp} the operator that projects a vector onto the plane with normal vector $\hat{\nu}$; specifically, P_{\perp} is given by $P_{\perp}X = X - \hat{\nu}(\hat{\nu} \cdot X)$.

Proposition: Suppose X^1 and X^2 are linearly independent vectors in the plane with normal \hat{n} . Then the vectors $P_{\perp}X^1$ and $P_{\perp}X^2$ are linearly independent if and only if $\hat{\nu} \cdot \hat{n} \neq 0$.

Proof: Suppose first that $\hat{\nu} \cdot \hat{n} \neq 0$. The issue of linear independence of $P_{\perp}X^1$ and $P_{\perp}X^2$ requires that we consider the condition $0 = c_1 P_{\perp}X^1 + c_2 P_{\perp}X^2 = P_{\perp}(c_1 X^1 + c_2 X^2)$. We denote by Y the linear combination $c_1 X^1 + c_2 X^2$. Then since $\hat{n} \cdot X^1 = 0 = \hat{n} \cdot X^2$, we also have $\hat{n} \cdot Y = 0$.

From the formula for P_{\perp} , the condition $0 = P_{\perp}Y$ is equivalent to

$$Y = \hat{\nu}(\hat{\nu} \cdot Y) \quad (34)$$

which also implies that $0 = \hat{n} \cdot Y = \hat{n} \cdot \hat{\nu}(\hat{\nu} \cdot Y)$. From this we see that $\hat{\nu} \cdot \hat{n} \neq 0$ implies $\hat{\nu} \cdot Y = 0$. But then we see from (34) that Y must be zero, which by the linear independence of X^1 and X^2 also implies that $c_1 = c_2 = 0$. Therefore $P_{\perp}X^1$ and $P_{\perp}X^2$ are linearly independent.

Next suppose that $\hat{\nu} \cdot \hat{n} = 0$. Then every vector X with $\hat{n} \cdot X = 0$ projects to a vector $Y = P_{\perp}X$ with the property that $\hat{n} \cdot Y = 0$ and $\hat{\nu} \cdot Y = 0$. All such vectors Y are multiples of each other; thus $P_{\perp}X^1$ and $P_{\perp}X^2$ are linearly dependent. QED

APPENDIX B NUMERICAL EXAMPLES

A. Straight Flight Path

The straight flight path we parameterized as $x_1 = 0, x_2 = s$; data $d(t, s)$ for it were generated by the formula

$$d(r, s) = r^{-1} \int V(r \cos \theta, s + r \sin \theta) d\theta \quad (35)$$

which was implemented with the Matlab “quad” routine. In all cases we used $Ns = 50$ points along the flight path, with $s_{min} = -20, s_{max} = 20$ so that the sampling interval was $ds = .8$. At each position on the flight path, we used $Nt = 50$ time samples and $ct_{min} = 3, ct_{max} = 30$, so that the sampling interval was $\Delta(ct) = .54$.

The formula for the image at coordinates (x_1, x_2) is

$$I(x_1, x_2) = \int e^{-i2k\sqrt{x_1^2+(x_2-s)^2}} 2kx_1 \int e^{i\omega t} d(t, s) dt d\omega ds. \quad (36)$$

This was implemented in Matlab by an FFT in the t variable, followed by multiplication by $2k = 2\omega/c_0$ (part of the Beylkin determinant) followed by an inverse FFT. This was followed by multiplication by x_1 (the other part of the Beylkin determinant) to obtain the backprojected data from one position s on the flight track. Nearest-neighbor interpolation was used to determine the appropriate data point to use for each pixel. Finally, contributions from all positions s are added together to build the image.

The reconstruction code ran in a matter of minutes for problems of size 100×100 . No attempt was made to optimize for speed.

B. Parabolic Flight Path

Parabolic flight paths $x_1 = ax_2^2$ were parameterized as $x_1 = as^2, x_2 = s$. Data for these paths were generated by implementing the formula

$$d(r, s) = r^{-1} \int V(as^2 + r \cos \theta, s + r \sin \theta) d\theta. \quad (37)$$

The formula for the reconstruction is

$$I(x_1, x_2) = \int e^{-i2k\sqrt{(x_1-as^2)^2+(x_2-s)^2}} 2k \times [2as(x_2-s) - (x_1-as^2)] \int e^{i\omega t} d(t, s) dt d\omega ds \quad (38)$$

which was implemented as discussed above.

ACKNOWLEDGMENT

The authors thank L. Ulander and his group for discussions and copies of their papers. They are also grateful to the Mathematical Sciences Research Institute for hosting them for the program on Inverse Problems during the fall of 2001.

REFERENCES

- [1] L.-E. Andersson, “On the determination of a function from spherical averages,” *SIAM J. Math. Anal.*, vol. 19, pp. 214–232, 1988.
- [2] B. Barber, “Theory of digital imaging from orbital synthetic aperture radar,” *Int. J. of Remote Sensing*, vol. 6, pp. 1009–1057, 1986.
- [3] G. Beylkin and R. Burrigge, “Linearized inverse scattering problems in acoustics and elasticity,” *Wave Motion*, vol. 12, pp. 15–52, 1990.

- [4] G. Beylkin, "Imaging of discontinuities in the inverse scattering problem by inversion of a causal generalized Radon transform," *J. Math. Phys.*, vol. 26, pp. 99–108, 1985.
- [5] N. Bleistein and R. A. Handelsman, *Asymptotic Expansions of Integrals*. New York: Dover, 1986.
- [6] N. Bleistein, J. K. Cohen, and J. W. Stockwell, *The Mathematics of Multidimensional Seismic Inversion*. New York: Springer, 2000.
- [7] M. Cheney, "A mathematical tutorial on Synthetic Aperture Radar," *SIAM Rev.*, vol. 43, pp. 301–312, 2001.
- [8] J. C. Curlander and R. N. McDonough, *Synthetic Aperture Radar*. New York: Wiley, 1991.
- [9] W. C. Carrar, R. G. Goodman, and R. M. Majewski, *Spotlight Synthetic Aperture Radar: Signal Processing Algorithms*. Boston, MA: Artech House, 1995.
- [10] C. Cafforio, C. Prati, and R. Rocca, "SAR data focusing using seismic migration techniques," *IEEE Trans. Aerosp. Electron. Syst.*, vol. 27, pp. 194–206, 1991.
- [11] L. J. Cutrona, "Synthetic Aperture Radar," in *Radar Handbook*, 2nd ed, M. Skolnik, Ed. New York: McGraw-Hill, 1990.
- [12] J. J. Duistermaat, *Fourier Integral Operators*. Boston, MA: Birkhauser, 1996.
- [13] C. Elachi, *Spaceborne Radar Remote Sensing: Applications and Techniques*. New York: IEEE Press, 1987.
- [14] J. A. Fawcett, "Inversion of N-dimensional spherical means," *SIAM J. Appl. Math.*, vol. 45, pp. 336–341, 1985.
- [15] G. Franceschetti and R. Lanari, *Synthetic Aperture Radar Processing*. New York: CRC, 1999.
- [16] S. E. Fisher, D. S. Weile, and E. Michielssen, "Pareto genetic algorithm design of log-periodic monopole arrays mounted on realistic platforms," *J. Electromagn. Waves Applicat.*, vol. 13, no. 5, pp. 571–598, 1999.
- [17] A. Gustavsson, P.-O. Frörlind, H. Hellsten, T. Jonsson, B. Larsson, G. Stenström, and L. M. H. Ulander, "Development and operation of the FOA CARABAS HF/VHF-SAR system," in *Proc. 4th Int. Workshop on Radar Polarimetry*, Nantes, France, July 13–17, 1998.
- [18] A. Grigis and J. Sjöstrand, *Microlocal Analysis for Differential Operators: An Introduction, London Mathematical Society Lecture Note Series*. Cambridge, U.K.: Cambridge Univ. Press, 1994, vol. 196.
- [19] H. Hellsten and L. E. Andersson, "An inverse method for the processing of synthetic aperture radar data," *Inv. Probl.*, vol. 3, pp. 111–124, 1987.
- [20] H. Hellsten, L. M. H. Ulander, A. Gustavsson, and B. Larsson, "Development of VHF CARABAS II SAR," *Proc. SPIE*, vol. 2747, pp. 48–60, 1996.
- [21] K. J. Langenberg, M. Brandfass, K. Mayer, T. Kreutter, A. Brüll, P. Felinger, and D. Huo, "Principles of microwave imaging and inverse scattering," *EARSel Advances in Remote Sensing*, vol. 2, pp. 163–186, 1993.
- [22] A. Louis and E. T. Quinto, "Local tomographic methods in SONAR," in *Surveys on Solution Methods for Inverse Problems*, D. Colton, H. W. Engl, A. K. Louis, J. R. McLaughlin, and W. Rundell, Eds. New York: Springer-Verlag, 2000.
- [23] A. S. Milman, "SAR imaging by $\omega - k$ migration," *Int. J. Remote Sens.*, vol. 14, pp. 1965–1979, 1993.
- [24] D. L. Mensa, *High Resolution Radar Cross-Section Imaging*. Norwood, MA: Artech House, 1991.
- [25] S. Nilsson, "Application of fast backprojection techniques for some inverse problems of integral geometry," in *Linköping Studies in Science and Technology*, 1997.
- [26] C. J. Nolan, "Scattering near a fold caustic," *SIAM J. Appl. Math.*, vol. 61, pp. 659–672, 2000.
- [27] F. Natterer, *The Mathematics of Computerized Tomography*. New York: Wiley, 1986.
- [28] C. J. Nolan and M. Cheney, "Synthetic Aperture Inversion," *Inv. Probl.*, vol. 18, pp. 221–236, 2002.
- [29] C. J. Nolan and W. W. Symes, "Global solution of a linearized inverse problem for the acoustic wave equation," *Commun PDE*, vol. 22, no. 5–6, 1997.
- [30] E. T. Quinto, "Singularities of the X-ray transform and limited data tomography in R^2 and R^3 ," *SIAM J. Math. Anal.*, vol. 24, pp. 1215–1225, 1993.
- [31] M. Soumekh, *Synthetic Aperture Radar Signal Processing With MATLAB Algorithms*. New York: Wiley, 1999.
- [32] ———, "Wavefront-based synthetic aperture radar signal processing," *Frequenz*, vol. 55, pp. 99–113, 2001.
- [33] M. Soumekh, D. Nobels, M. Wicks, and G. Genello, "Signal processing of wide-bandwidth and wide-beamwidth P-3 SAR data," *IEEE Trans. Aerosp. Electron. Syst.*, vol. 37, pp. 1122–1141, 2001.
- [34] F. Trèves, *Basic Linear Partial Differential Equations*. New York: Academic, 1975.
- [35] ———, *Introduction to Pseudodifferential and Fourier Integral Operators, Volumes I and II*. New York: Plenum, 1980.
- [36] C. W. Therrien, *Discrete Random Signals and Statistical Signal Processing*. Englewood Cliffs, NJ: Prentice-Hall, 1992.
- [37] L. M. H. Ulander, H. Hellsten, and G. Stenström, "Synthetic-aperture radar processing using fast factorized backprojection," preprint, Dec. 2000.
- [38] L. M. H. Ulander and P.-O. Frörlund, "Ultra-wideband SAR interferometry," *IEEE Trans. Geosci. Remote Sensing*, vol. 36, pp. 1540–1550, Sept. 1998.
- [39] L. M. H. Ulander and H. Hellsten, "Low-frequency ultra-wideband array-antenna SAR for stationary and moving target imaging," in *Proce. Conf. SPIE 13th Annu. Int. Symp. Aerosense*, Orlando, FL, Apr. 1999.
- [40] D. R. Wehner, *High-Resolution Radar*, 2nd ed. Norwood, MA: Artech House, 1995.

Clifford J. Nolan received the B.Sc. degree in applied math from the National University of Ireland, Galway; the M.Sc. in theoretical physics from Trinity College, Dublin, Ireland, and the Ph.D. in applied mathematics from Rice University, Houston, TX, in 1997.

He was a National Science Foundation postdoctoral fellow at the University of Washington from 1997 to 2000 and an Assistant Professor of mathematics at Rensselaer Polytechnic Institute, Troy, NY, from 2000 to 2001. Since 2001, he has been a Lecturer in applied mathematics at the University of Limerick, Limerick, Ireland.

Margaret Cheney received the B.A. degree in mathematics and physics from Oberlin College, Oberlin, OH, in 1976, and the Ph.D. in mathematics from Indiana University, Bloomington, in 1982.

She was a Postdoc at Stanford University, Stanford, CA, from 1982 to 1984 and an Assistant Professor of mathematics at Duke University, Durham, NC, from 1984 to 1988. Since 1988, she has been at Rensselaer Polytechnic Institute, Troy, NY, where she is Professor of mathematics. She has held visiting appointments at NYU's Courant Institute (1987–1988) at the Minnesota Institute for Mathematics and Its Applications (1994–1995 and 1997), the Berkeley Mathematical Sciences Research Institute (2001), and the Naval Air Warfare Center Weapons Division (2002). Most of her work has been on the inverse problems that arise in quantum mechanics, acoustics, and electromagnetic theory. From 1995 to 1997 she served as Editor-in-Chief of the *Journal Of Applied Mathematics*; she is currently a member of the editorial boards of *Journal Of Applied Mathematics* and *Inverse Problems*.

Dr. Cheney has received several awards, including the Office of Naval Research Young Investigator Award in 1986, a National Science Foundation Faculty Award for Women in Science and Engineering in 1990, and the Lise Meitner Visiting Professorship at Lund Institute of Technology in 2000. She was a member of the Rensselaer Impedance Imaging team that received the 1993 ComputerWorld Smithsonian Award in the Medicine category. She is a member of the SIAM board of Trustees, of the Electromagnetics Academy, and is a Fellow of the Institute of Physics.